

Ultrashort pulse propagation in air-silica microstructure fiber

Brian R. Washburn and Stephen E. Ralph
School of Electrical and Computer Engineering
Georgia Institute of Technology, Atlanta, GA 30332, USA
stephen_ralph@ece.gatech.edu

Robert S. Windeler
OFS Fitel Laboratories, Murray Hill, NJ 07974, USA

Abstract: The unique dispersive and nonlinear properties of air-silica microstructure fibers lead to supercontinuum generation at modest pulse energies. We report the results of a comprehensive experimental and numerical study of the initial stages of supercontinuum generation. The influence of initial peak power on the development of a Raman soliton is quantified. The role of dispersion on the spectral development within this pre-supercontinuum regime is determined by varying the excitation wavelength near the zero dispersion point. Good agreement is obtained between the experiments and simulations, which reveal that intrapulse Raman scattering and anti-Stokes generation occur for low power and short propagation distance.

©2002 Optical Society of America

OCIS Codes: (190.4370) Nonlinear Optics, Fibers; (230.3990) Microstructure Devices; (320.7110) Ultrafast Nonlinear Optics; (000.4430) Numerical Approximation and Analysis;

References

1. J. K. Ranka, R. S. Windeler, and A. J. Stentz, "Visible continuum generation in air-silica microstructure optics fibers with anomalous dispersion at 800 nm," *Opt. Lett.* **25**, 25-27 (2000).
2. K. W. DeLong, R. Trebino, J. Hunter, and W. E. White, "Frequency-resolved optical gating with the use of second-harmonic generation," *J. Opt. Soc. Am. B* **11**, 2206-2215 (1994).
3. M. D. Feit and J. A. Fleck, "Light propagation in graded-index optical fibers," *Appl. Opt.* **17**, 3990-3998 (1978).
4. G. P. Agrawal, *Nonlinear Fiber Optics*. (Academic Press, 1995), Chap. 2.
5. K. J. Blow and D. Wood, "Theoretical description of transient stimulated Raman scattering in optical fibers", *IEEE J. Quantum Electron.* **25**, 2665-2673 (1989).
6. B. R. Washburn, S. E. Ralph, P. A. Lacourt, J. M. Dudley, W. T. Rhodes, R. S. Windeler, and S. Coen, "Tunable near-infrared femtosecond soliton generation in photonic crystal fibers," *Electron. Lett.* **37**, 1510-1511 (2002).
7. F. M. Mitschke and L. F. Mollenauer, "Discovery of the soliton self-frequency shift," *Opt. Lett.* **11**, 659-661 (1986).
8. J. M. Dudley, L. Provino, N. Grossard, H. Maillotte, R. S. Windeler, B. J. Eggleton, S. Coen, "Supercontinuum generation in air-silica microstructured fibers with nanosecond and femtosecond pulse pumping," *J. Opt. Soc. Am. B* **19**, 765-771 (2002).
9. S. Coen, A. Chau, R. Leonhard, J. D. Harvey, J. C. Knight, W. J. Wadsworth, P. S. J. Russell, "Supercontinuum generation by stimulated Raman scattering and parametric four-wave mixing in photonic crystal fibers," *J. Opt. Soc. Am. B* **19**, 753-64 (2002).
10. J. Herrmann, U. Grebner, N. Zhavoronkov, A. Husakou, D. Nickel, J. C. Knight, W. J. Wadsworth, P. S. J. Russell, and G. Korn, "Experimental evidence for supercontinuum generation by fission of higher-order solitons in photonic fibers," *Phys. Rev. Lett.* **88**, 173901-173903 (2002).
11. N. Akhmediev and M. Karlsson, "Cherenkov radiation emitted by solitons in optical fibers," *Phys. Rev. A* **51**, 2602-2607 (1995).

1. Introduction

The large effective nonlinearity and near-visible zero group-velocity-dispersion (GVD) wavelength make air-silica microstructure fibers (ASMF) an ideal system for investigating and exploiting optical nonlinearities in fused-silica. In fact, supercontinuum generation has

been demonstrated with these fibers using ultrashort pulses of ~1 nJ energy [1]. The role of each distinct nonlinear effect during supercontinuum generation may be strongly dependent on the excitation pulse properties and the fiber dispersion. Quantifying this dependence is required if the generated supercontinuum is to be exploited. To this end, we have performed an experimental and numerical investigation of ultrashort pulse propagation in ASMF as a function of input peak power, P_0 , and excitation center wavelength, λ_0 . This study provides an understanding of the fundamental nonlinear processes that dominate the spectral evolution in the low power ($P_0 < 1000$ W) pre-supercontinuum regime, thus providing insight into the transition to the supercontinuum regime.

The ASMF used consists of a hexagonal lattice of holes with diameter ~1400 nm in a fused-silica fiber. The core is a solid region of diameter ~1600 nm at the center of the lattice. Hyperbolic secant² pulses of 110 fs duration (intensity full-width at half maximum) generated from a Kerr-lensed mode-locked Ti:sapphire laser were launched into a 1.7 m length of ASMF. The specific fiber geometry, which is described in Ref. [1], yields a zero GVD wavelength at $\lambda_{ZGVD} = 767$ nm. Second-harmonic-generation frequency-resolved optical gating (SHG FROG) [2] was used to measure the input pulse intensity and phase. The resulting output light was analyzed using a background-free intensity autocorrelation measurement and a spectrometer.

Numerical solutions to the nonlinear Schrödinger equation (NLSE) were found using the split-step Fourier method [3] with the FROG retrieved field as $E(z=0, t)$. Care was taken to include the full temporal response of the third-order electric susceptibility in the NLSE used for our simulations [4]:

$$\frac{\partial E(z, t)}{\partial z} = \underbrace{-\frac{\alpha}{2} E}_{\text{Absorption}} - \underbrace{\left(\sum_{m=2} \beta_m \frac{i^{m-1}}{m!} \frac{\partial^m}{\partial t^m} \right) E}_{\text{Dispersion}} + \underbrace{i\gamma \left[(1-f_R) \left(\underbrace{|E|^2 E}_{\text{SPM}} - \frac{2i}{\omega_0} \frac{\partial}{\partial t} (|E|^2 E) \right) + f_R \left(1 + \frac{i}{\omega_0} \frac{\partial}{\partial t} \right) \left(\underbrace{E \int_0^\infty h_R(t') |E(z, t-t')|^2 dt'}_{\text{SRS}} \right) \right]}_{\text{Nonlinearity}}, \quad (1)$$

where z is the direction along the fiber length, α is the absorption coefficient, β_m is the m^{th} dispersion coefficient, γ is the effective nonlinearity, ω_0 is the pulse center frequency, f_R is the relative strength of the Raman contribution and $E(z, t)$ is the pulse complex temporal envelope. The nonlinear susceptibility has two dominant time scales: a fast component that contributes to self-phase modulation (SPM) and four-wave mixing (FWM), and a slow component that is the origin of stimulated Raman Scattering (SRS). Since the initial pulse duration for the experiment was ~100 fs, the fast component of the response is treated as instantaneous while the non-instantaneous portion of the response is written in terms of the SRS temporal response $h_R(t)$. An approximate form of $h_R(t)$ is used for our simulations [5]. Thus, Eq. (1) includes the effects of absorption, higher-order dispersion, SPM, SRS and self-steepening. Specific values were $\alpha \sim 10$ dB/km, $\gamma \sim 0.07$ (W m)⁻¹ and the β_m were evaluated for each λ_0 using the measured dispersion [1]. For instance, $\beta_2 = -2.5 \times 10^{-6}$ fs²/nm, $\beta_3 = 6.0 \times 10^{-5}$ fs³/nm, $\beta_4 = -3.1 \times 10^{-5}$ fs⁴/nm, $\beta_5 = 7.4 \times 10^{-5}$ fs⁵/nm and $\beta_6 = -6.2 \times 10^{-4}$ fs⁶/nm for $\lambda_0 = 780$ nm. The simulation temporal and spectral resolution was typically $\delta t = 0.85$ fs and $\delta \lambda = 0.31$ nm respectively.

2. Intrapulse Stimulated Raman Scattering and Anti-Stokes Generation

The behavior of the Raman soliton is sensitive to input power and dispersion, thus modeling it accurately is a strenuous test of the simulation. Furthermore, the input peak powers for observing the Raman soliton span the pre-supercontinuum regime to the supercontinuum regime. The nonlinearities involved are therefore important in both regimes. Figure 1 shows

the development of the Raman soliton as a function of P_0 for $\lambda_0=780$ nm. The presence of the Raman soliton is due to intrapulse SRS [6] which is related to the soliton self-frequency shift [7]. Both the numerical and measured spectra show the formation of a weak, shorter-wavelength ($\lambda < \lambda_0$) peak, called here the anti-Stokes component, at $\lambda_{as} \sim 720$ nm. Anti-Stokes generation has been observed for similar initial pulse durations in Ref. [8], and has been attributed to coupling between SRS and parametric FWM [9]. Also, anti-Stokes generation has been explained in terms of the fission of higher-order solitons into blue-shifted nonsolitonic spectral components [10], a process related to Cherenkov radiation in optical fibers [11]. Although we do not propose a physical model for anti-Stokes generation, our simulations complement the referenced work by showing the explicit dependence of the anti-Stokes wavelength on the value of the third-order dispersion coefficient β_3 .

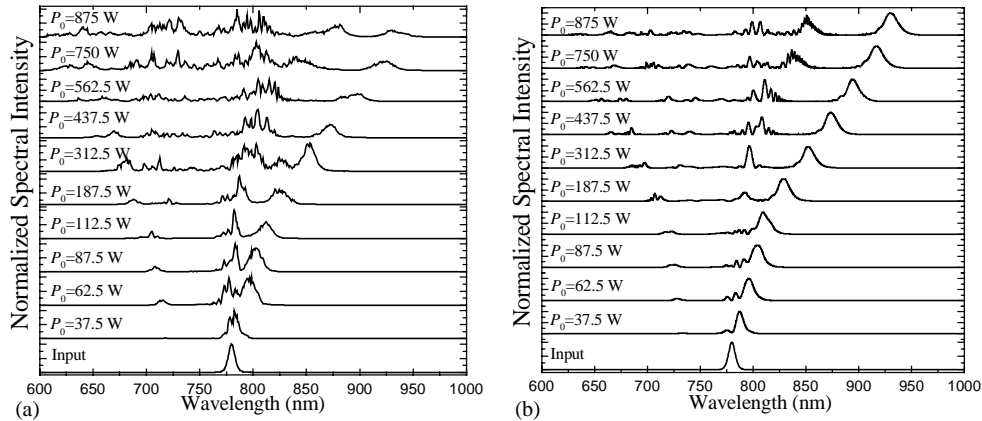


Fig. 1. (a) Measured spectra as a function of peak power, P_0 , for an input pulse centered at $\lambda_0=780$ nm. (b) The corresponding simulated spectra as a function of P_0 .

Numerical simulations show that both intrapulse SRS and anti-Stokes generation are observed after a short propagation distance. This is illustrated in the movie of spectral development with propagation distance (z) in Fig. 2. For short distances the spectrum exhibits features due to SPM. Later, the Raman soliton and anti-Stokes component are formed after $z=0.289$ m. The soliton is further red-shifted due to continuous intrapulse SRS. Interestingly,

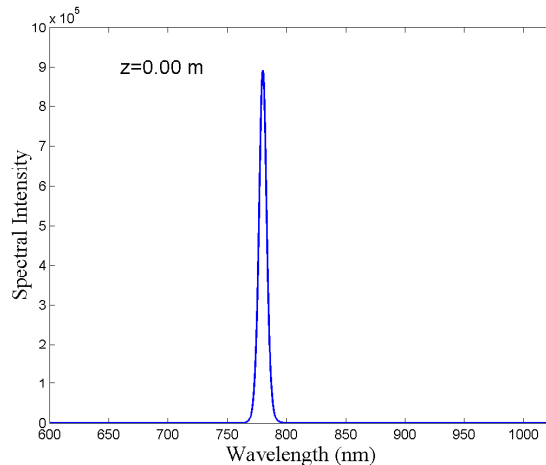


Fig. 2. (810 kB) Spectral propagation movie of an initial 110 fs sech^2 pulse at $\lambda_0=780$ nm with $P_0=440$ W, through 1.7 m of ASMF. Each frame is the current spectrum at position z in the fiber.

at $z=1.139$ m more anti-Stokes components emerge from the initial anti-Stokes component and are further blue-shifted as the Raman soliton is red-shifted.

The temporal development for the same initial pulse also illustrates the formation of the Raman soliton. As seen in Fig. 3, the initial 110 fs pulse is compressed to 12 fs at a distance of $z=0.187$ m. This short pulse duration and higher peak power is well handled by the simulation as evidenced by the excellent numerical and experimental agreement of Fig. 1. The final soliton duration after 1.7 m is 60 fs, which is delayed from the residual pulse by 3300 fs. Both the numerical soliton duration and separation correspond well to intensity autocorrelation measurements [6].

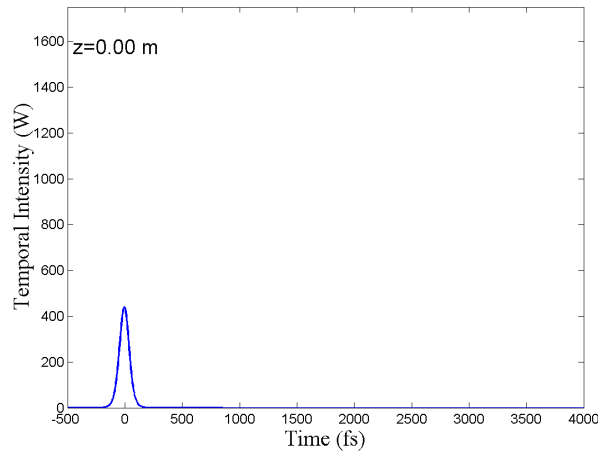


Fig. 3. (802 kB) Temporal propagation movie of an initial 110 fs sech^2 pulse at $\lambda_0=780$ nm with $P_0=440$ W, through 1.7 m of ASMF. Each frame is the temporal envelope at position z in the fiber.

3. Behavior of the Anti-Stokes Components

The precise excitation center wavelength is of importance for supercontinuum generation since FWM components may be phase matched for $\lambda_0 \approx \lambda_{ZGVD}$. The sensitivity to λ_0 is a direct consequence of the effects of dispersion. As seen in Fig. 4(a), the observed anti-Stokes components became more intense as λ_0 was decreased from 820 nm to 770 nm. This observation is consistent with the numerical simulations of Fig. 4(b).

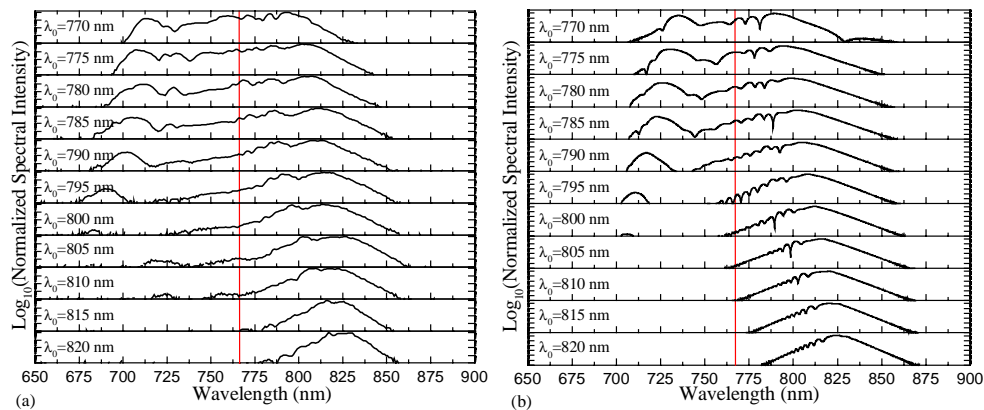


Fig. 4. (a) Measured spectra taken with $P_0=76$ W while varying λ_0 , from 770 nm to 820 nm. The zero GVD wavelength is indicated by the red vertical line. An anti-Stokes component appears as λ_0 is decreased to λ_{ZGVD} . (b) Simulated spectra as a function of λ_0 for $P_0=76$ W.

The influence of the center wavelength on the anti-Stokes component is revealed by the solutions to the NLSE. Figure 5 shows the spectral development of a 110 fs input pulse with $\lambda_0=806$ nm and $P_0=440$ W, which is to be compared with Fig. 2. This center wavelength is one of the longest that generates an observable anti-Stokes component. Again, intrapulse SRS is prevalent, however, the anti-Stokes component formed after $z=0.187$ m is of lower intensity compared to the $\lambda_0=780$ nm results.

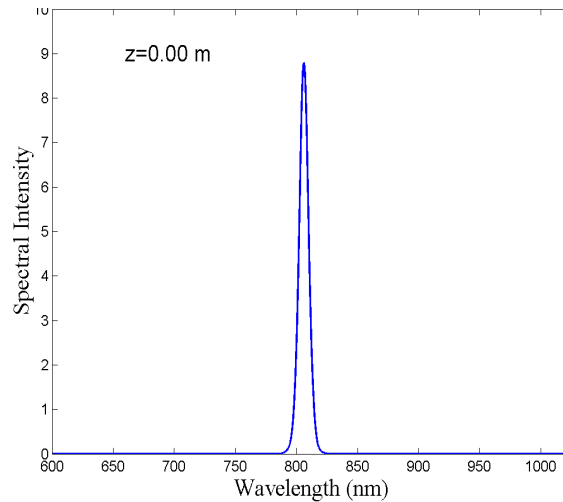


Fig. 5. (808 kB) The propagation of an initial 110 fs sech^2 pulse at $\lambda_0=806$ nm with $P_0=440$ W, through 1.7 m of ASMF. Each frame is the current spectrum at position z in the fiber.

The question arises whether the new spectral components are due to phase-matched FWM terms. The formation of the anti-Stokes component may be due to partially degenerate FWM since the component appears as the input center wavelength is shifted to λ_{ZGVD} . For partially degenerate FWM a Stokes component (in addition to the Raman soliton) is expected along with the anti-Stokes component. The wavelength of the Stokes component can be determined using energy conservation. For example, the $\lambda_0=770$ nm spectrum of Fig. 4 has an anti-Stokes component at $\lambda_{as}=714$ nm. The corresponding Stokes component should be near $\lambda_s=860$ nm, however, there is no experimentally observed feature at this wavelength. In fact, the phase mismatch is not zero using $\lambda_{as}=714$ nm, $\lambda_0=770$ nm and $770 \text{ nm} < \lambda_s < 860 \text{ nm}$. Thus, the generation of the anti-Stokes component is not due to partially degenerate FWM since the observed spectral components do not satisfy energy and momentum conservation. It is possible that the anti-Stokes component may be a result of other FWM processes. Evidence for other origins of anti-Stokes generation is the focus of our ongoing research.

The numerical simulations show that the early formation of the anti-Stokes component is strongly dependent on the third-order dispersion coefficient (cubic dispersion). As seen in Fig. 6(a), the wavelength of the anti-Stokes component is significantly altered by varying β_3 while keeping all other β_m constant. These observations are consistent with the conclusions of Ref. [11]. The simulations illustrate that the absence of β_3 prevents the formation of the anti-Stokes component. In fact, for $\beta_3 = -\beta_{3,ASMF}$ there is no anti-Stokes component but a new Stokes component appears.

The simulations also demonstrate that SRS has little influence on the early formation of the anti-Stokes component. However, anti-Stokes components that form after $z=1.139$ m are more sensitive to SRS. This is illustrated in Fig. 6(b), where the top plot shows the spectrum at $z=0.30$ m while the bottom plot is at $z=1.70$ m. For $z=0.30$ m the presence of SRS has little impact on the initial anti-Stokes component, while at $z=1.70$ m SRS contributes to the later anti-Stokes components.

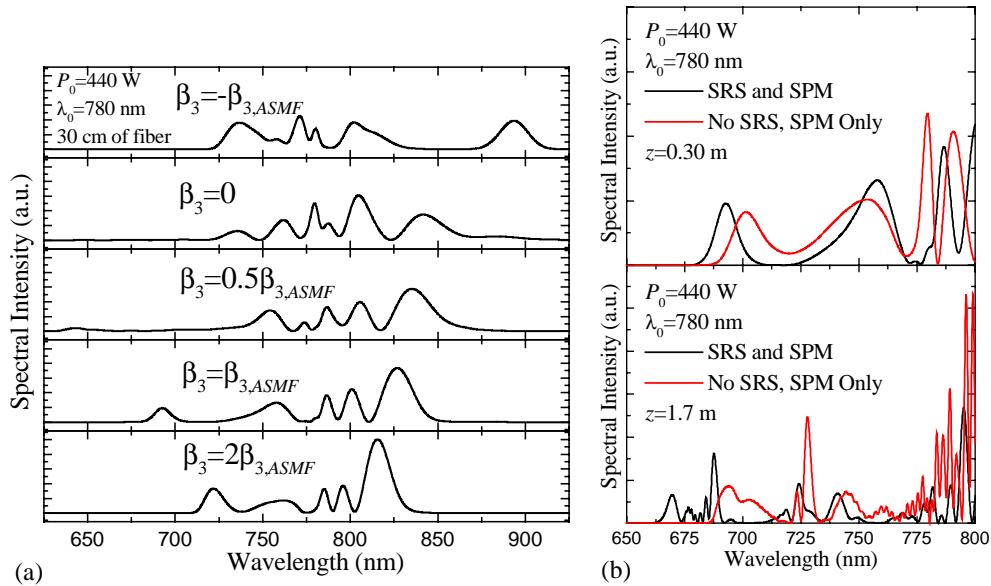


Fig. 6. (a) The wavelength dependence of the anti-Stokes component with varying third-order dispersion β_3 . The term $\beta_{3,ASMF}$ represents the actual third-order dispersion coefficient of the ASMF. The anti-Stokes wavelength was red-shifted for increasing β_3 while all other β_m remain constant. Note also the anti-Stokes component was missing for $\beta_3=0$ and a new Stokes component is present for $\beta_3=-\beta_{3,ASMF}$. (b) Anti-Stokes components for simulations with and without SRS. The top plot shows the spectrum at $z=0.30$ m while the bottom plot is at $z=1.70$ m.

4. Conclusions

We have experimentally observed and numerically confirmed that multiple nonlinear mechanisms are occurring simultaneously during pulse propagation in ASMF. Both intrapulse SRS and anti-Stokes generation occur early in fiber propagation. Furthermore, the influence of the excitation center wavelength on anti-Stokes generation has been shown for center wavelengths near the zero GVD wavelength. The formation of the anti-Stokes component is not due to partially degenerate FWM, however it is strongly dependent on the specific fiber cubic dispersion. These results are of significance for the pre-supercontinuum regime since the anti-Stokes component contributes largely to the short-wavelength portion of the spectrum while intrapulse SRS contributes to the long-wavelength portion. Clearly, these results further the understanding of the nonlinear processes that occur within the supercontinuum regime.

Acknowledgments

The authors are grateful to John Dudley, Stéphane Coen and Pierre Lacourt for informative discussions.